UTILIZATION OF DIGITAL IMAGE CORRELATION TO IDENTIFY FAILURE MECHANISMS OF HALLUX VALGUS IMPLANTS

A

Thesis

Presented to
the faculty of the School of Engineering and Applied Science
University of Virginia

Submitted in partial fulfillment of the
requirements for the degree of Master of Science

by

Victor Shen

December, 2022

APPROVAL SHEET

This

Thesis

is submitted in partial fulfillment of the requirements for the degree of

Master of Science

Author: Victor Shen

This Thesis has been read and approved by the examing committee:

Advisor: Xiaodong Li

Committee Member: Baoxing Xu

Committee Member: David Green

Accepted for the School of Engineering and Applied Science:

Jennifer L. West, School of Engineering and Applied Science

December 2022

ACKNOWLEDGMENTS

I would like to first thank my family and colleagues for their continued support throughout my time here at the University of Virginia. I would also like to thank Dr. Xiaodong Li for his excellent mentorship during my time as a graduate student and sharing his passion for innovation with me. I would next like to thank Dr. Joseph Park for his insight and mentorship on the projects that we collaborated on during my time at UVa.

I have to thank Lisa Actis and Joseph Ritz for their support and belief in the work that we carry out here at the University of Virginia and funding two projects. I would also like to thank DePuy Synthes/BioMedical Enterprises for providing the hallux valgus implants utilized and described in this work.

ABSTRACT

Identification of potential failure mechanisms is key for any material whether the application is in the medical industry or pertains to matters of national security. In order to reveal the failure mechanisms, tests must be conducted in a safe, accurate and consistent manner. In this work, we utilized in-situ 3D Digital Image Correlation (3D-DIC) to study implant performance and deformation under simulated motion as well as track gap displacement of the 1st tarsometatarsal (TMT) joint following surgical intervention for locking plate and nitinol staples using innovative anthropomorphic bend test setups. The focus is divided into two phases.

The first phase is the characterization of bone-implant behavior using a PCF sawbone model. PCF sawbone is readily available polyurethane foam that can mimic cancellous bone density and be machined to have the same complex geometry of human bone. An asymmetric three-point bend setup was utilized along with 3D-DIC to study implant performance. A relationship was established between each implant's performance and how plantar, towards the heel, the implant was placed.

The second part of this thesis dealt with using cadaveric samples and inclusion of biological tissue. Cadaveric samples are critical due to their clinical relevance and understanding how variation in bone density can affect implant hardware. A modified cantilever bend setup was utilized alongside 3D-DIC to study both implant performance against bone density. Strain concentrations identified on the nitinol staple bridge indicated potential areas of failure in the pursuit of understanding the capacities of each implant under simulated early weight bearing.

Our results demonstrate that the locking plates are less affected by plantar location and provide more initial stability and resistance against gapping under load but are unable to recover compression throughout repetitive loading as seen with the nitinol staple technology. DIC

methodology combined with the innovative asymmetric bend tests could lead to a paradigm shift in materials used for implants and how implants are biomechanically tested for early weight bearing protocols.

TABLE OF CONTENTS

LIST OF FIGURES

LIST OF TABLES

Table # Page

NOMENCLATURE

3-D	Three Dimensional
CMOS	Complementary metal-oxide semiconductor
DFS	Deviation From Symmetry
DIC	Digital Image Correlation
Dorsal	Top of the foot
E	Young's Modulus
F	Applied Load
HVA	Hallux Valgus Angle
I	Moment of Inertia
IMA	Intermetatarsal Angle
L	Distance from first to second load point
Lateral	Away from the middle
M	Bending Moment
Medial	Towards the middle or center
MTP	Metatarsophalangeal
Plantar	Bottom of the foot
r	Radius of the rod
TMT	Tarsometatarsal
Transverse	Bisecting into top and bottom
x	Location on the beam
y	Distance from the beam midpoint
σ	Stress at any point in the rod

Chapter 1: Introduction

1.1 Background on Hallux Valgus

Hallux valgus, or bunion deformity, is one of the most common foot problems that patients present to foot and ankle specialists. Bunions occur in up to 35.7% of people over the age of 65 and 23% of people between the ages of 18 and 65 [1,34]. There are various grades of hallux valgus, beginning with mild cases where the HVA is 20 degrees and increasing to severe cases with a HVA of nearly 40 degrees [2]. In 2018 alone there were 430,002 bunionectomies performed and with an average price quote of $18,332 that would imply a financial burden of nearly $8 billion per year [3,34]. Even a conservative estimate of failure of arthrodesis, outcome studies indicated that up to 15% of Lapidus procedures result in non-union, leading to another 64,000 revision procedures to address these non-unions [4,34] for an added cost of just over $1 billion.

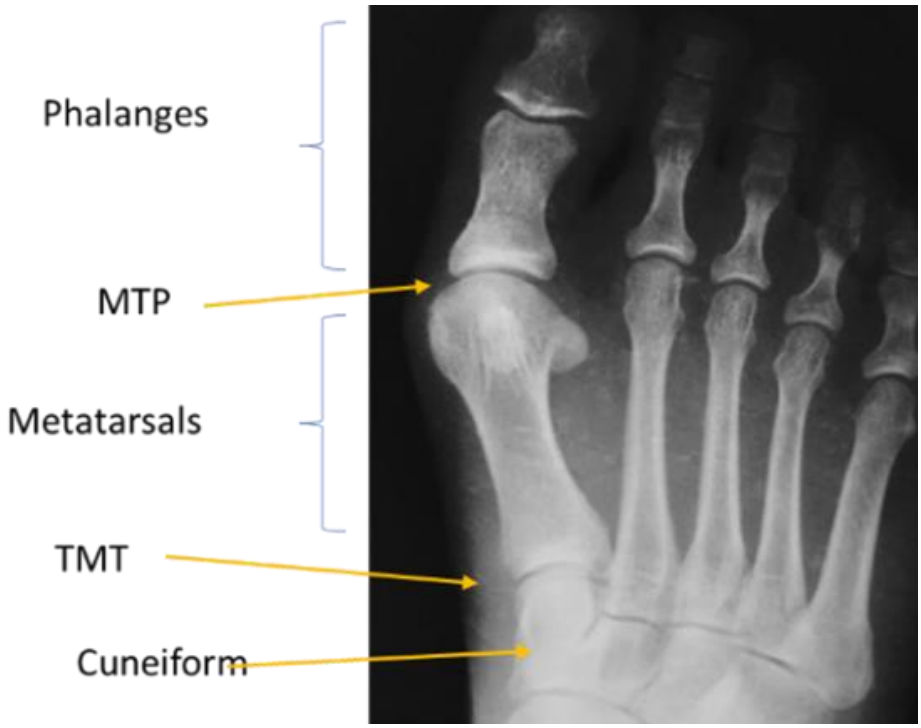

Figure 1. Bone joint and segments labeled on a human right foot

Bunions typically occur due to constant pressure on the MTP joint, causing a misalignment of the bones in the big toe as well as the bone bump. This pressure has a myriad of sources, ranging from an imbalance in extrinsic and intrinsic foot muscles and ligamentous structures [5], poor gait mechanics, poor foot structure, excessive amount of time spent standing as well as poor fitting or narrow shoes. The bunion is characterized by the lateral deviation of the hallux or big toe at the MTP joint towards the other toes with an additional lateral deviation of the metatarsal at the TMT joint as seen in Figure 1.

The key to advancing the science of medical implants is performing biomechanical testing to understand implant performance and deformation at the bone-implant interface. However, anthropomorphic test setups are needed to provide better clinical insight when using sawbone or cadaveric samples to avoid nonunion. Sawbones have the benefit of being manufactured to consistent geometries and therefore are a more uniform and consistent sample [6]. On the other hand, cadaveric bone has the added benefit of cortical and cancellous bone interacting with biological tissue. This thesis is targeting that gap and aims to add to the wealth of knowledge in the field.

1.2 Prior Work on Corrective Techniques

There are a myriad of medical procedures each with their respective associated hardware used in orthopedic procedures. The first corrective technique for hallux valgus was described in 1871 and since then, well over 100 unique procedures have been detailed. Conservative techniques such as soft tissue procedures like the McBride or Smith Peterson intervention have been used in the past but due to risk of causing hallux varus, the pointing of the big toe away from the other toes, those procedures have ceased [7]. Osteotomies, such as the chevron [5] or

Figure 2. Using HVA and IMA to diagnose severity

scarf [7] among others, are also conservative techniques as they are typically reserved for mild cases of hallux valgus. Although severe cases of hallux valgus may require more radical techniques utilizing fusion or fixation of the joint such as an arthroplasty or arthrodesis that incorporate hardware. However, the arthroplasty procedure has fallen out of favor due to lack of success in bone union but the arthrodesis procedure is still utilized especially for cases of hallux valgus with osteoarthritis [7].

The hardware selected can vary based on the patient's medical history as well as the surgeon's preference and experience. To determine the optimal corrective technique for each patient's bunion, radiographs are taken of the patient's feet to determine the IMA and HVA as shown in Figure 2. The IMA is determined by drawing lines that bisect the first metatarsal and second metatarsal. The HVA takes into account the line that bisects the proximal phalanx of the first ray and the line bisecting the base of the first metatarsal. The HVA and IMA have been identified through multiple studies to be the most reliable among the eight possible radiographic

measurements with respect to the ability to correctly evaluate hallux valgus [8, 9].

The hallux valgus correction procedure that we chose for this work is the Lapidus arthrodesis procedure, which was first described in 1934 by Paul W. Lapidus [10]. The Lapidus procedure is designed to solve metatarsocuneiform joint hypermobility and hallux valgus by realigning and fusing the 1st TMT joint [11]. The Lapidus arthrodesis has been shown to have low nonunion rates even as a corrective procedure in patients [12] but variations of the procedure such as those that use an intermetatarsal screw have only been shown to be effective in cadaveric studies [13].

1.3 **Scope of the Thesis**

In this work, failure mechanisms of hallux valgus Lapidus arthrodesis implants will be investigated using DIC at room temperature in both sawbone and cadaver models. Anthropomorphic test setups combined with the in-situ optical measurement methodology allow for unique opportunities to study implant behavior in a simulated patient environment. The primary objective was to better understand the nitinol staple and locking plate implants in simulated motion otherwise known as early weight bearing, which is a significant contributor to failure. The secondary objective was to determine localized strain concentrations on implants and provide feedback on areas of concern. Parts of this work spanning from Chapter 1 to Chapter 6 have been published in the following journal papers.

[34] Shen VC, Bumgardner CH, Actis L, Ritz J, Park J, Li X. "3D Digital Image Correlation Evaluation of Arthrodesis Implants." Clinical Biomechanics 71(1), 29-36. 2020.

[41] Shen VC, Bumgardner CH, Actis L, Park J, Moyer D, May-Nikstaitis K, Li X. "In Situ Deformation of First Tarsometatarsal Arthrodesis Implants with Digital Image Correlation: A

Cadaveric Study." The Minerals, Metals & Materials Society 74(9), 3357-3366. 2022. [Springer Nature]

Chapter 2: Overview of Digital Image Correlation and Bend Testing

2.1 Digital Image Correlation Overview

3D-DIC is an optical method that uses stereoscopic images to capture and track points on a material surface. Stereoscopic images are pictures taken by cameras at slightly different angles such that, when they are combined together, create a sense of depth. Unlike conventional strain gauge measurements, 3D-DIC is non-destructive technique that uses high resolution optical images with a random speckle pattern to quantify full field deformation and strain on the surface of a sample[14]. When coupling 3D-DIC with two high resolution digital CMOS cameras, out-

Parameter	Test Specifications
DIC Image Acquisition Rate	4Hz
Software	Correlated Solutions Vic-3D
Cameras	2x 5 megapixel CMOS (Point Grey)
Lenses	50mm compact lens (Schneider)
Subset Size	41* pixels
Step Size	10* pixels
Calibration	In-Plane calibration with 4mm grid

Figure 3. Example of parameters used for DIC capture and analysis

of-plane deformation can be measured with a resolution down to 1/20,000th of camera-sample distance [15,34,41]. This enables DIC to capture quantitative measurements of strain distributions across the surface of bone, including local concentrations around implant sites and joints [16,17,18,19,34].

In order to perform DIC, a 2D calibration target is used to define the geometric relationship between the cameras and the sample (i.e. the angles between the camera and distances between sample and cameras). A random speckle patterned is applied to provide images that can be correlated between a reference (unloaded sample) and a loaded sample. The correlation VIC-3D was used to compute the resultant full field deformation and strain maps of the sample during testing. Typically, the high-contrast pattern is established with a white background supplemented with black speckles. However, if the material surface has sufficient texturing or simply needs a speckling applied to an evenly colored surface, then the DIC will still be able to track displacement. One critical factor is that DIC needs sufficient directional lighting to prevent any reflection or shadow onto the material surface, which can be picked up by the cameras as oversaturated pixels and ultimately affect the quality in resultant 3D-DIC measurements.

In order to measure the region of interest, the two high-resolution cameras must be positioned in a way to have overlapping fields of coverage. Then the lens of each camera is focused onto the sample surface and tune the exposure time to optimize the contrast of the speckling on the sample. Next a calibration is performed through the VIC-3D software using a uniform grid with known distance between each speckle; in this work a 4mm grid was used, to determine the spatial relationship between the two high-resolution cameras. The overlapping spatial locations are identified on each 2D camera image, and the resultant 3D map is produced. Lastly, for each experiment, a base noise level is established using a set of images with no load applied to the sample to verify no artificial strain or displacement is being picked up by the high-resolution cameras prior to the experiment beginning.

Once images are loaded into VIC-3D software, they can be analyzed using specific subset and step sizes. Subsets are important because they act as the grid window within the image for where the software is focusing the image analysis, and there must be enough speckles within each window to create a unique signature. Step size is important as it serves to tell the software how fine of a comb to use as it progresses through the subset. If the subset size is too small then the software will not be able to distinguish between other subsets and there will be a loss in DIC coverage on the material surface. However, if the subset size is too large then the computation time may increase unless the step size is also increased accordingly but that will decrease spatial resolution. Therefore, there is a constant back and forth between computational time and fullness of the 3D map.

2.2 **Bend Testing**

Three-, four-point, and cantilever bend tests are commonly used due to their ability to replicate robust measurements. Three-point bend tests provide a more realistic distribution of internal loading than four-point bend tests but at the cost of potential indentation on the tissue of the sample during loading [20]. A review by Kubiak et al. found that biomechanical testing for locking plates has historically favored utilization of three-point bend tests [21]. However, recent studies have employed four-point bend tests when comparing implant performance of medial locking plates with a compression screw or crossed screws in cadaveric samples, as well as nitinol staples in sawbone blocks [22,23,24,34]. One key factor that affects which test is utilized is whether the geometry is consistent between samples.

Chapter 3: Implant Evaluation Methodologies

Implant- and procedure-specific mechanical tests are performed to answer several questions such as how load configurations affect strain, joint gapping, and the implant

effectiveness. Another often weighed question is how evaluation differs when using an anatomically correct foot model juxtaposed against a simplified geometric model such as a foam block. Full-field 3D-DIC measurements are well suited to resolve strain fields across the complex geometry of bone specimens [34,41]. Several previous studies that conducted implant/bone loading tests used rectangular polyurethane foam blocks rather than anatomically correct versions of the bone. Although foam blocks are able to simulate cancellous bone and have uniform dimensions, for providing more surface area for the implant to purchase onto, it is important to recognize that regions of the first ray may be wider or narrower than what is expected in a specimen foam block. Therefore, uniform foam blocks cannot accurately represent the strain experienced by the curved/irregular bone, implant, or interface seen in cadaveric specimens [20,24,25,26,27,34]. Even within cadaveric samples, studies would isolate the specific joint by stripping all of the tissue which removes the inherent stability and excise the joint for implantation and subsequent testing [22,28,41].

The recorded performance of the implants are somewhat restricted to the specific loading configuration of the specimens; namely, we suspect the commonly utilized three- or four-point bend configurations, intended for geometrically uniform specimens, are not an accurate method for bend testing of geometrically complex, biological specimens. We propose in this work an asymmetric, three-point bend testing protocol, which integrates the known loading modes and allows realistic deformation of the toe to better simulate in-vivo forces during weight bearing. Given the length of the 1st metatarsal from the heel and the proximity of the heel to the tibia, we believe that the forces imposed on the 1st TMT joint are better characterized using an asymmetric three-point bending fixture [29,34]. Asymmetric four-point bend fixtures have been attempted on polyurethane foams of varying densities, but the results were inconclusive with issues of

localized crushing leading to undesired failure modes in specimens [30,34]. In contrast, we anticipate that the asymmetric, three-point bend protocol will allow for a natural deformation of the toe, preventing crushing [34].

3.1 **Asymmetric Three Point Bend Testing**

We note that this work is the first experimental study of toe deflection using 20 PCF solid rigid polyurethane bone specimens with various arthrodesis implants with realistic load configuration. Thus, our aim is to develop a fundamental understanding of the stress-strain state along with the first ray under these conditions and of the boundary conditions. In future studies, we expected that these conditions will elucidate the understanding of the material behavior and will eventually empower more accurate numerical and analytical approaches to account for the complexities in the model. For this fundamental experiment, the bone region from the toe tip to the heel was modeled in a simplified form as a cylindrical beam in which the beam deflection formula explains that the further away the point load is from the neutral axis, the larger the deflection and the resultant plantar gapping. Under the proposed asymmetric three-point load configuration, two points of loading are applied to the calcaneus and cuneiform bones to stabilize the toe. The third point of loading is applied to the plantar first metatarsal head where the sesamoids would be located (Figure 4c). Thus, the distribution of loads replicates actual loading of the toe to better simulate weight bearing forces [29,34].

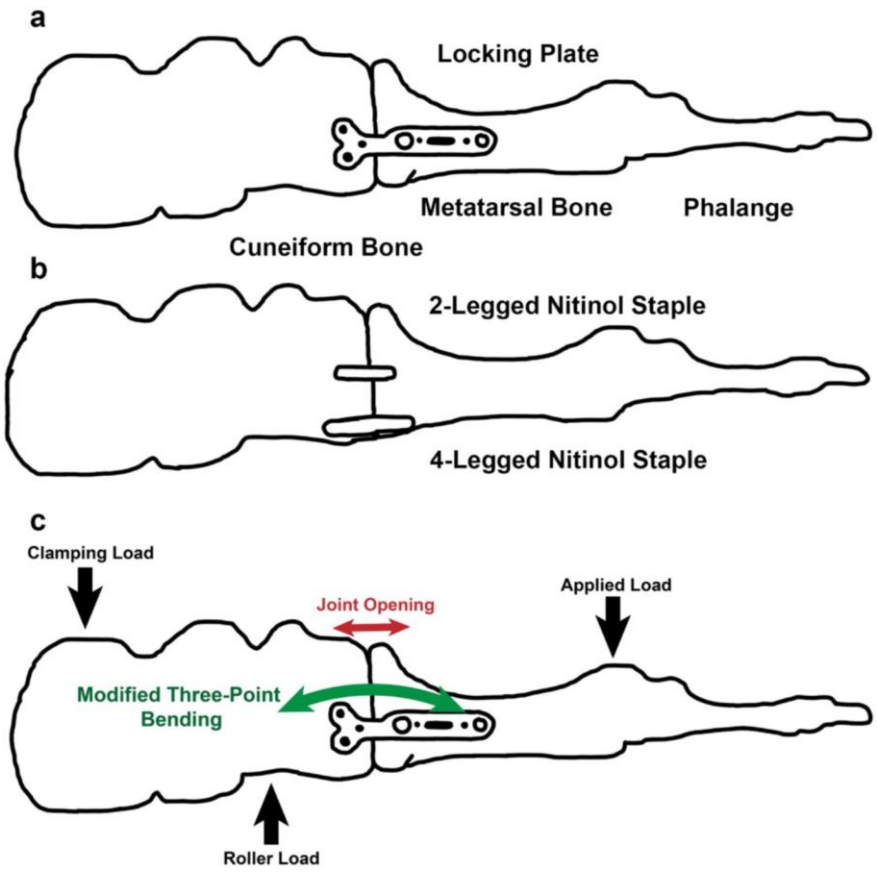

Figure 4. Schematic of the a) locking plate and b) nitinol staples in how they would be subjected to the c) asymmetric three-point bend test for sawbone samples [34]

The proposed, asymmetric, three-point bend test is designed to replicate actual loading of the medial ray for more realistic and meaningful examination of implant devices like those in Figure 4a and 4b. The asymmetric load configuration represents a deviation from prior studies

[34]. To quantify the deformation and strain under various load configurations, a simplified experiment was conducted using aluminum rods as seen in Figure 5.

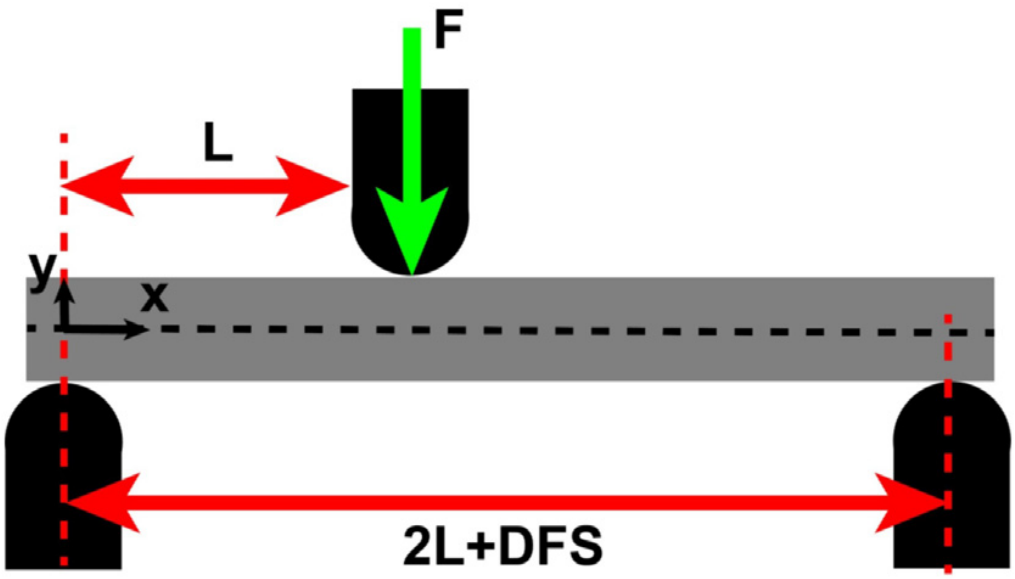

Figure 5. Schematic of the asymmetric three-point bend validation test setup [34]

Three rods were notched to simulate joint gap displacement of the foot model relative to the stiffness of the beam and relative to the load configuration. This validation study was essential to justify the use of the asymmetric load configuration for the implant study. The purpose of the implant is to close the joint gap, but we needed to first understand how the load configuration itself impacted the gap displacement. From a beam-in-bending standpoint, we assumed the bending moment increased the further the loads are from the gap, thus increasing gap opening. From this validation study, we began to understand how the load configuration would affect gap opening and the local stress state at the gap. Again, we assumed this fundamental understanding may be translated to the foot-implant model even though the sawbone foot model had a lower stiffness. Since the elastic stress concentration factor is larger than 4, the fatigue stress is similar between unnotched and notched specimens [31,34]. Rods

were loaded in symmetric three-point and four-point configurations (Figure 6a, b) and in asymmetric three-point configurations to characterize the full-field deformation that is representative of the various types of biomechanical testing (Figure 6c–e) [34].

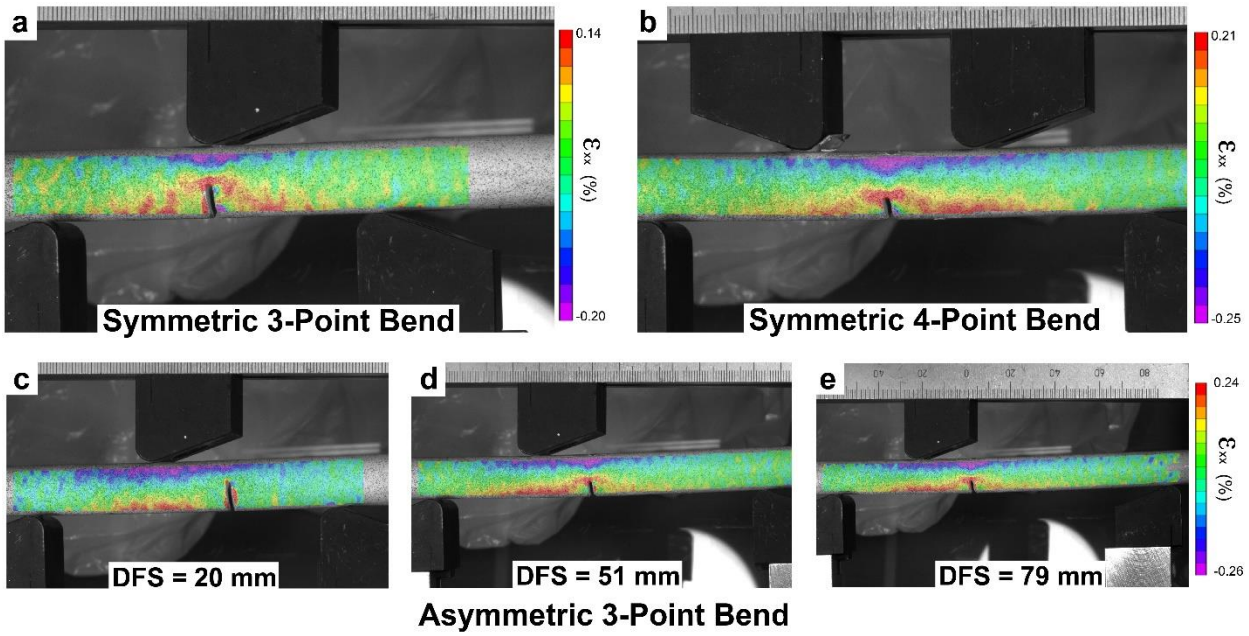

Figure 6. 3D-DIC strain profiles of various aluminum rod validation tests. Symmetric (a) three-point and (b) four-point bend tests were performed to validate strain measurements while asymmetric tests, with DFS values of (c) 20, (d) 51, and (e) 79 mm, illustrated the impact of asymmetric loading on gap opening displacement. [34]

Strains measured via DIC could be coupled with stress calculations to identify the modulus. Stress along any point of the rod may be described by $\sigma = \frac{M(x)y}{I}$, where M(x) is the bending moment along the beam length "x", y is the distance away from the neutral axis, and I is the moment of inertia. The moment of inertia of a rod is $I = \frac{\pi r^4}{4}$, where r is the radius of the rod. The maximum stress associated with bending will occur at the farthest point from the neutral axis, when y = r. Therefore, the bending moment must be calculated for a rod with a symmetric or asymmetric load configuration. It can be shown that the moment can be described by $M(x \leq L) = \frac{Fx(L+FDS)}{2L+DFS}$ and $M(x \geq L) = FL(1 - \frac{x}{2L+DFS})$, where F is the applied load, L is the

distance from the first to second load point, and DFS, or deviation from symmetry, is the distance from which the third load point is moved beyond a symmetric location of 2 L from the first load point (Figure 5). The testing was performed on an ADMET eXpert 2611 table-top universal testing machine up to a load of 3500 N. The 3D-DIC strain profiles demonstrated the Euler- Bernoulli linear strain profile across the cross-section of the aluminum bars, showing the transition from compression at the top to tension along the underside of the bar [32,34]. Subsequently, the strain data was analyzed to extrapolate the stress-strain behavior and the Young's modulus, calculated as 69.7 GPa (with a standard deviation of 1.8 GPa), well within established literature value of 68.9 GPa [33,34]. During each test, the notch was monitored with DIC to track the opening and closing of the gap during loading and unloading; the relative effect on the displacement of the gap opening due to the load configuration could then be assessed. These configurations included the symmetric three-point and four-point bend arrangements as baseline tests (Figure 6a, b). To replicate the proposed asymmetric load configuration, four configurations were evaluated. In each of these asymmetric configurations, the first and second loading points were set 37mm apart (Figure 7a), based on the geometric spacing of the calcaneus and cuneiform bones of the foot model. The notch was located at 62mm to align with the location the joint between the cuneiform and first metatarsal. The third loading point was located at positions moving out from a point of symmetry; i.e., it was located at 37mm from the second load point plus some specified DFS value. We considered DFS values of 0, 20 (Figure 6c), 51 (Figure 6d), and 79mm (Figure 6e). The DFS value of 51mm aligned the third load point in alignment with the plantar first metatarsal head, the site of actual loading on the toe; the other DFS values were selected to check the effect of variation from this location. The gap spacing displacement measured with a symmetric three- and four-point configuration was 0.074 and

0.065mm respectively. In contrast, the gap spacing displacement from the asymmetric configuration began at 0.02mm and increased to 0.09mm with increasing deviation from symmetry (Figure 7a, b). This trend reflects the increasing moment of bending experienced along this section of the beam due to the increasing moment arm. Furthermore, this trend also highlights the critical importance of modeling not just the specimen but also the load configuration after the actual conditions experienced by the foot. The gap opening displacement at the notch for the 51mm DFS location was 0.085, higher than the displacement in the symmetric load configuration tests, indicating that symmetric configurations may not expose the specimen to the full deformation and stress the actual bone experiences [34].

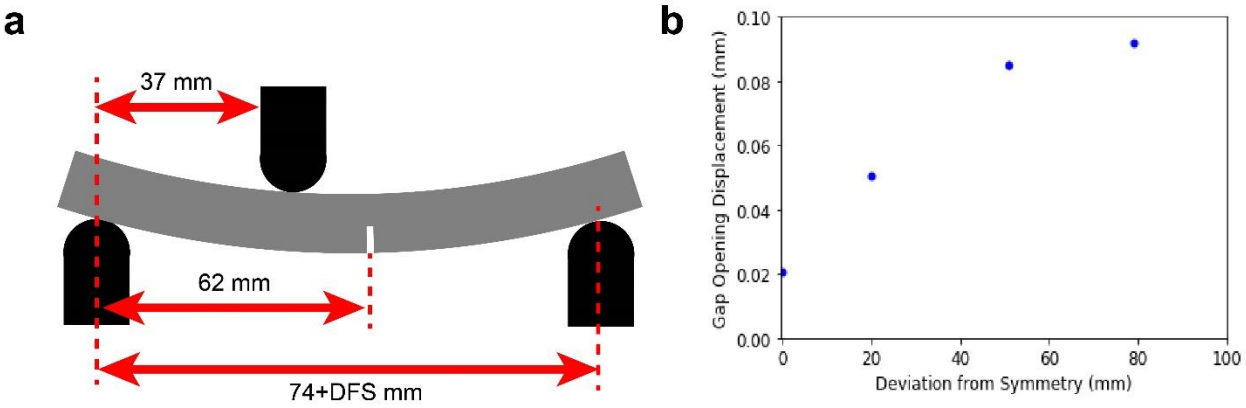

Figure 7. Gap opening based on DFS distance. Values obtained from the DIC analysis. (a) Schematic of the load configuration of the validation tests on notched aluminum (b) The gap opening displacement plotted against DFS values. [34]

3.2 **Modified Cantilever Bend Testing**

In this work we also propose a modified cantilever bend test where the load point is consistently applied to the sesamoids under the 1st metatarsal head rather than at the toe tip. In a simplified form, the foot can be modeled as a beam, in which the beam deflection formula explains that the further the point load is from the fixed end, the larger the deflection and resultant plantar gapping. The cantilever bend setup utilized the same underlying principles as

the asymmetric three-point bend setup from the sawbone phase and was better suited to account for the fixation of bone and soft tissue [34,41]. The fixed end of the cantilever encapsulated the ankle and the heel, while the first ray was the free end and the sesamoids were the primary point of contact for loading (Figure 8). The moment arm varied according to each cadaveric sample, but would generally be measured from the talus to the TMT joint.

In order to specifically isolate the 1st TMT, a surgical cut was made across the 2nd through 5th rays mid-way through the metatarsals. A skin flap was excised above the first TMT to allow for removal of the peritoneal layer, hardware implantation through the arthrodesis procedure, and eventual speckling of the implant-bone surface. This allowed for an anthropomorphic loading while simulating weight-bearing forces. The tissue acted as natural boundary conditions to keep the joint constrained [41].

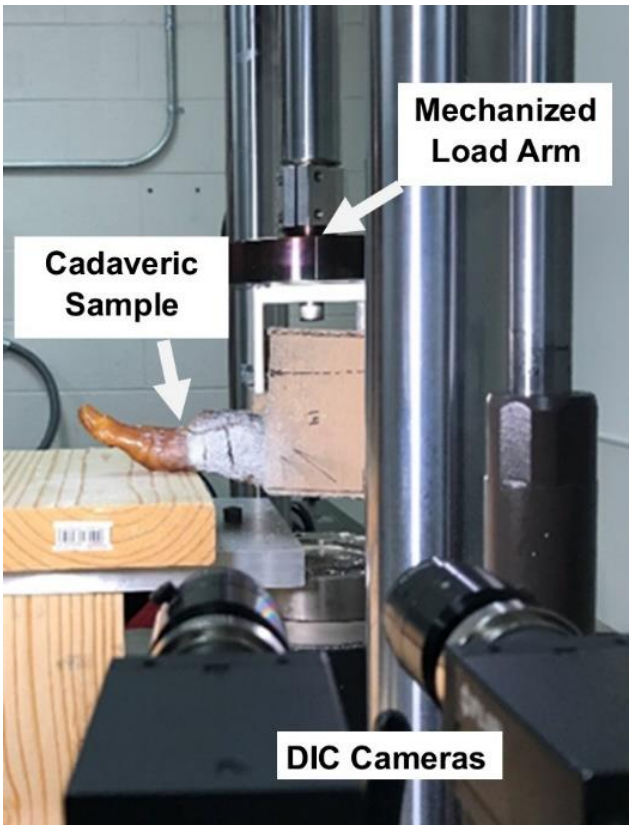

Figure 8. Modified cantilever bend setup for cadaveric samples [41]

Chapter 4: Overview of Hallux Valgus Lapidus Arthrodesis Technique

4.1 Lapidus Arthrodesis Correction

The Lapidus procedure as mentioned earlier is a technique that realigns and fuses the 1st TMT joint using hardware and a period of non-weight bearing to allow for bone union. First, the joint was exposed, reduced, and fixated in preparation for hardware implantation. Pilot holes were drilled using guides associated with the respective implant hardware. Next, hardware was implanted to mimic a Lapidus procedure through simulated arthrodesis by a fellowship trained, Board Certified Orthopedic Foot and Ankle Surgeon [34,41].

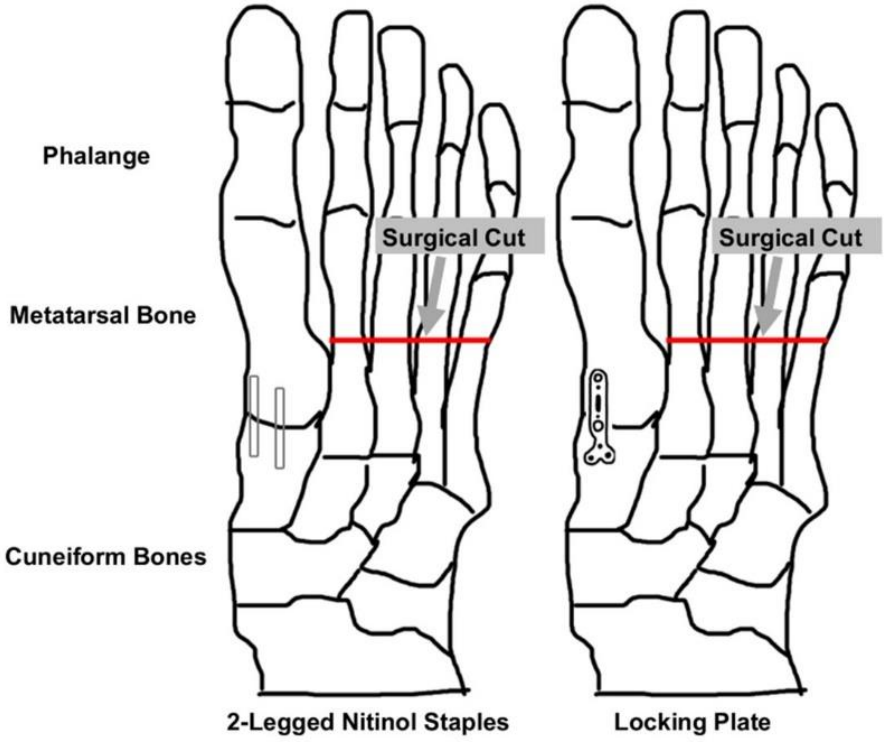

Figure 9. Isolation of 1st TMT through surgical removal of 2nd through 5th rays [41]

4.2 Types of Implants Used

Two types of implants were utilized in this work; a locking plate and lag screw combination construct as well as a dual nitinol staple construct. The locking plate has grown in popularity due to their ability to be "bridge" plates that span across the TMT joint space and due

to being manufactured out of stainless steel or titanium, have excellent biocompatibility and mechanical resistance to deformation. Nitinol staples are also growing in popularity as an implant for early weight bearing protocols due to their superelastic material properties and being able to adapt to gapping and resorption in vivo while maintaining excellent biocompatibility [23].

During the Sawbone phase, the nitinol staples used a 4 leg EL-2520S4 staple that was inserted dorsally, and a 2 leg EL-1818S2 staple that was inserted medially across the TMT joint modeled in Figure 4b. For the lag screw and locking plate construct, a 4.0 cannulated screw was placed dorsally across the lateral half of the TMT joint, and a 4-hole dorsomedial T-plate was used to neutralize the lag screw modeled in Figure 4a [34].

For the cadaveric phase, the same locking plate and lag screw combination was used, but the dual nitinol staple construct used two 2-legged staples. For the lag screw and locking plate system, a 4.0 cannulated screw was placed retrograde across the lateral half of the TMT joint from the metatarsal to the medial cuneiform, and a 4-hole dorsomedial T-plate was used to neutralize the lag screw modeled in Figure 10a. For the nitinol staple constructs, an EL-2020S2 staple was inserted dorsally, and an EL-1818S2 staple was inserted medially, across the TMT joint modeled in Figure 10b [41].

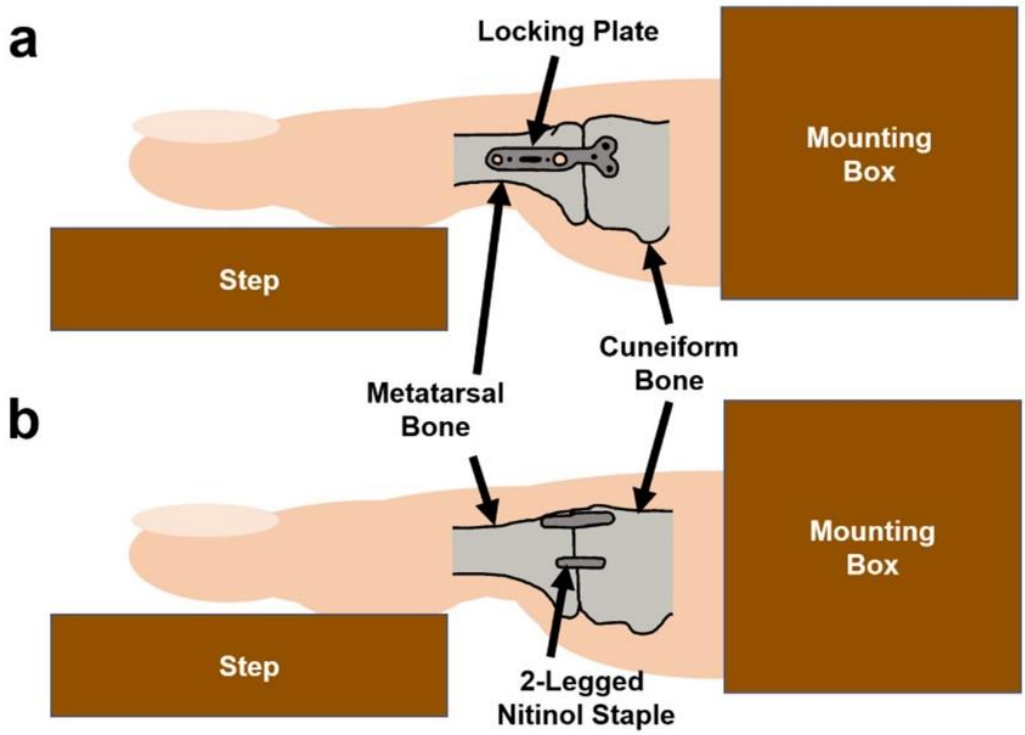

Figure 10. Schematic of a) locking plate hardware and b) nitinol staple hardware [41]

4.3 **Sample Preparation Protocol**

The Sawbone phase represented a simulation of loading on the foot model and implants and makes two key improvements over recent works: (i) the use of an anatomically correct model of the foot and (ii) an asymmetric loading frame to simulate realistic loading of the foot. The implanted medial column constructs were loaded onto the Bruker Universal Mechanical Tester (UMT) (Figure 11) with a three-point bend setup; the talus and navicular region were immobilized by an O-ring clamp while the cuneiform was placed on top of a cylindrical roller. The load was applied to the plantar aspect of the 1st MTP joint via a mechanized arm to complete the three-point setup. Loading conditions were kept the same across each specimen, loading was cycled at a frequency of 0.66 cycles per minute using the preset speed rate of 0.01 mm/s of the Bruker UMT. Each cycle was loaded up to 50 N for 100 iterations based on maximum pressure values under the first TMT published by Luger in 1999 [34,35]. To prevent any major

differences in machine compliance, all tests were carried out in rapid succession and conducted at room temperature (~70 °F). The foot specimens were prepared for DIC with an applied speckle pattern using matte black and white paint. To collect in-situ, three-dimensional strain fields, two FLIR Grasshopper 3 GS3-U3-50S5M-C digital CMOS cameras were mounted on a horizontal beam atop a tripod and paired with 50mm Schneider lenses (Figure 11). The 50mm lenses were selected based on the desired field of view for each specimen and to ensure that a single speckle was composed of at least 3 pixels for sufficient oversampling and reduction of erroneous measurements. Baseline images without any load were taken to quantify system error and noise; an error magnitude of 10^{-5} mm/mm was observed consistently across all samples tested and note this error was more than two orders of magnitude below the strains measured during loading. During the testing, images were captured at a rate of 2 Hz. For the nitinol staple samples, the subset size and step size were 31 pixels and 9 pixels, respectively. The locking plate samples utilized a subset size and step size of 41 pixels and 11 pixels, respectively [34].

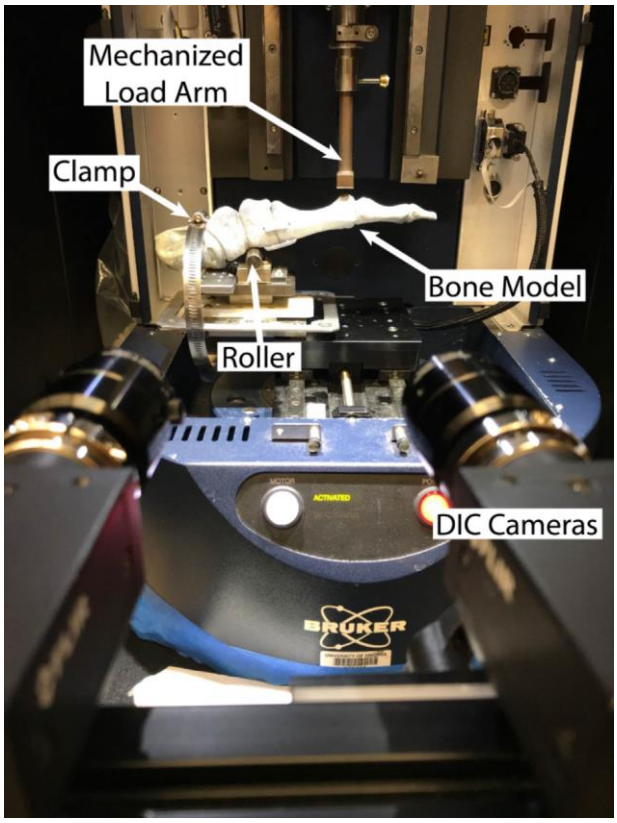

Figure 11. Asymmetric bend test on the Bruker UMT with sawbone sample loaded [34]

For the cadaveric phase, after partial removal of the 2nd through 5th rays at the level of proximal metatarsal shafts as demonstrated in Figure 9, the implanted medial column constructs were loaded into the MTS 858 Bionix (Figure 8) in a cantilever bend setup. The calcaneus was removed, leaving the distal foot intact, including the talus and cuboid. All soft tissues were stripped to the level of the talus and cuboid to allow for maximum bone surface area to bond with the Fast Cast 709 resin (Goldenwest Manufacturing, Inc.) without covering the surgical site [36,41]. Transverse K-wires were then placed across the cuboid and talus to further enhance bony fixation for testing. The resin was cast into identically constructed boxes where two 3-cm-wide holes were drilled to mount the cadaver specimen into the MTS. The mounted cadaver specimens were displaced cyclically to simulate the step-off phase of the walking cycle, with the load applied to the plantar aspect of the 1st MTP joint. The loading conditions were kept the same

across each specimen, and the loading was cycled up to 50 N for 100 iterations, based on maximum pressure values under the first TMT [35,41]. To prevent any major differences in machine compliance, all tests were carried out in rapid succession and conducted at room temperature [24,41]. The foot samples were prepared for DIC with an applied speckle pattern using matte black and white paint at least an hour before testing, in order to allow the paint to dry sufficiently without losing significant moisture in the bone to the atmosphere. Two FLIR Grasshopper 3 GS3-U3-50S5M-C digital CMOS cameras were mounted on a horizontal beam atop a tripod, and paired with 50mm Schneider lenses, so that 3D strain fields could be collected in situ (Figure 8). This specific lens was selected based on the desired field of view for each specimen, and to ensure that a single speckle was composed of at least 3 pixels for sufficient over-sampling and reduction of erroneous measurements. Baseline images without any load were taken and analyzed via commercial DIC software (VIC-3D; Correlated Solutions) to quantify system error and noise. An error magnitude of 10^{-5} mm/mm was observed consistently across all samples tested; we note that this error was more than two orders of magnitude below the strains measured during loading, indicating that the measurement error was insignificant relative to the measurement strains. During testing, images were captured at a rate of 4 Hz. For the nitinol staple samples, the subset size and step size were 51 pixels and 8 pixels, respectively. The locking plate samples utilized a subset size and step size of 53 pixels and 7 pixels, respectively [41].

Chapter 5: Failure Mechanisms of Hallux Valgus Implants

A common failure mode associated with implants is loss of fixation at the bone-implant interface from cyclical loading and motion. Locking plates suffer in particular from lag screw pullout, which is where the load and motion at the joint cause the screw to back out of the

implantation site. Now, with the addition of locking screws to assist in cumulative compression of the locking plate with the lag screw, Lapidus procedures have improved rates of union. Staples have been used in previous history but due to being constructed with pure titanium, the staples lacked the structural stability to maintain compression during loading events. As mentioned earlier, with SMA staples like nitinol there has been a return to favor for implantation during Lapidus procedures partially due to their markedly shorter installation period compared to locking plates. Malunion can also occur if the joint is not prepared properly or if the patient has specific vices such as smoking, unhealthy diet that can lead to weight gain [34,37].

5.1 **Localized Strain Regions**

For the sawbone phase of this work, each type of implantation had three samples tested. All tests sustained the full 100 iterations of loading to 50 N and relaxation without any instances of catastrophic failure of either the implants or the bone substitute. For locking plate samples, the bone substitute experienced peak strains of 0.0302 and 0.0234 mm/mm near the plantar region of the TMT. The implant measured various maximum strains due to the difficulty of placing the hardware in the exact same location of each sample. Of the three samples, the peak strain found on the implant was 0.0139 and 0.0174 mm/mm in the ε_{xx} and ε_{yy} directions respectively. For the nitinol staple samples, the maximum strains of bone substitute were found to be 0.0198 and 0.0134 mm/mm near the interface between the implant and the bone. However, the nitinol implants showed relative uniformity and measured 0.0062 and 0.0036 mm/mm in the ε_{xx} and ε_{yy} directions respectively (Figure 12). In both cases, the bone substitute experienced more of the deformation and strain, particularly around the implant-bone interface. The deformations observed with the locking plate regularly exceeded those when using the nitinol staples, indicating that the comparatively flexible design of the nitinol staple allows for a steady flex of

the joint. On the contrary, the locking plate resisted flexure, concentrating all deformation along the implant-bone interface. Over time, the deformation of the bone and implant experienced variability in the measurements, but none that indicated plastic deformation [34].

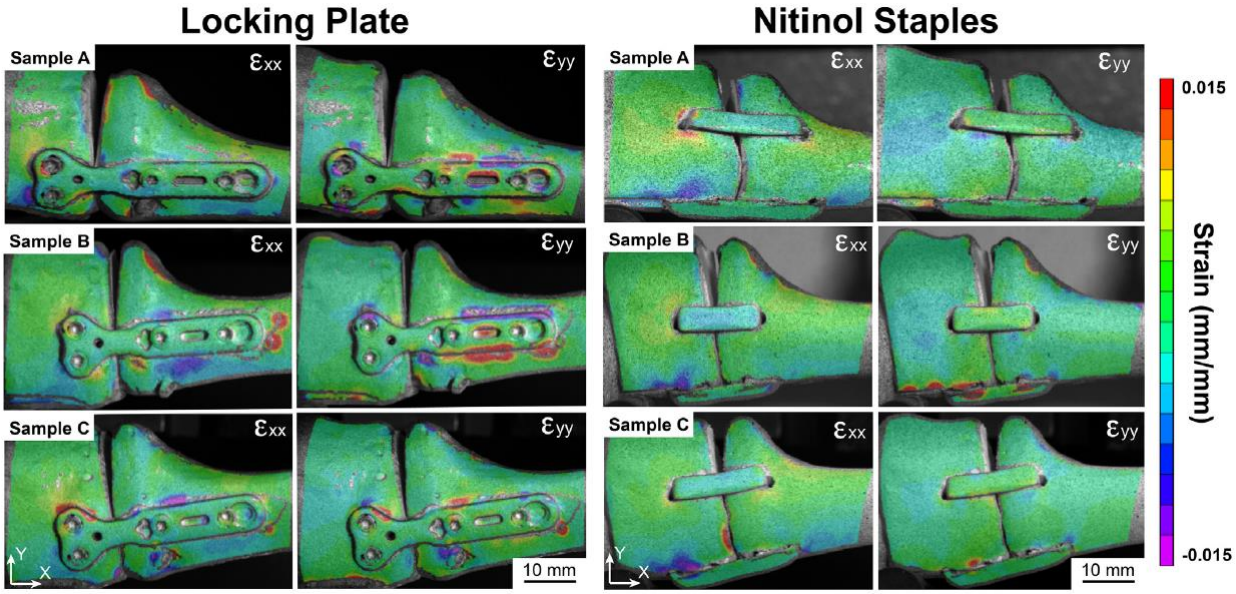

Figure 12. 3D-DIC strain map of sawbone implants after anthropomorphic loading [34]

The purpose of the cadaver phase of this work was to more closely simulate the early postoperative period, where the patient is enrolled in an early weight-bearing protocol. The modified foot structure also introduced a load profile consistent with more realistic loading of the foot. Resulting DIC strain profiles revealed a fairly homogenous profile along the bone and locking plate structures. Figure 13 shows that local tensile and compressive strain concentrations, up to magnitudes as high as 51%, were confined to the bone–implant interfaces, indicating that these local strain concentrations may be artificially increased by relative displacement of the interface itself rather than of the implant or bone. The DIC profiles indicated that the locking plate provided superior rigid support to secure the joint than the nitinol staples; this function was highlighted by the homogeneous distribution of low strain along the implant–bone interface. In

contrast, the nitinol staple allowed some flexure of the implants to accommodate motion of the foot, yet allowed for recovery of contact at the joint. The higher peak strains observed with the nitinol staples showed that the comparatively flexible design of the nitinol staple requires further investigation into whether those stress points are of concern or are still within the operational range of the nitinol material. Both implant constructs could be considered for arthrodesis patients enrolling in an early weightbearing protocol based on the average maximum gap sustained during cyclical loading [41].

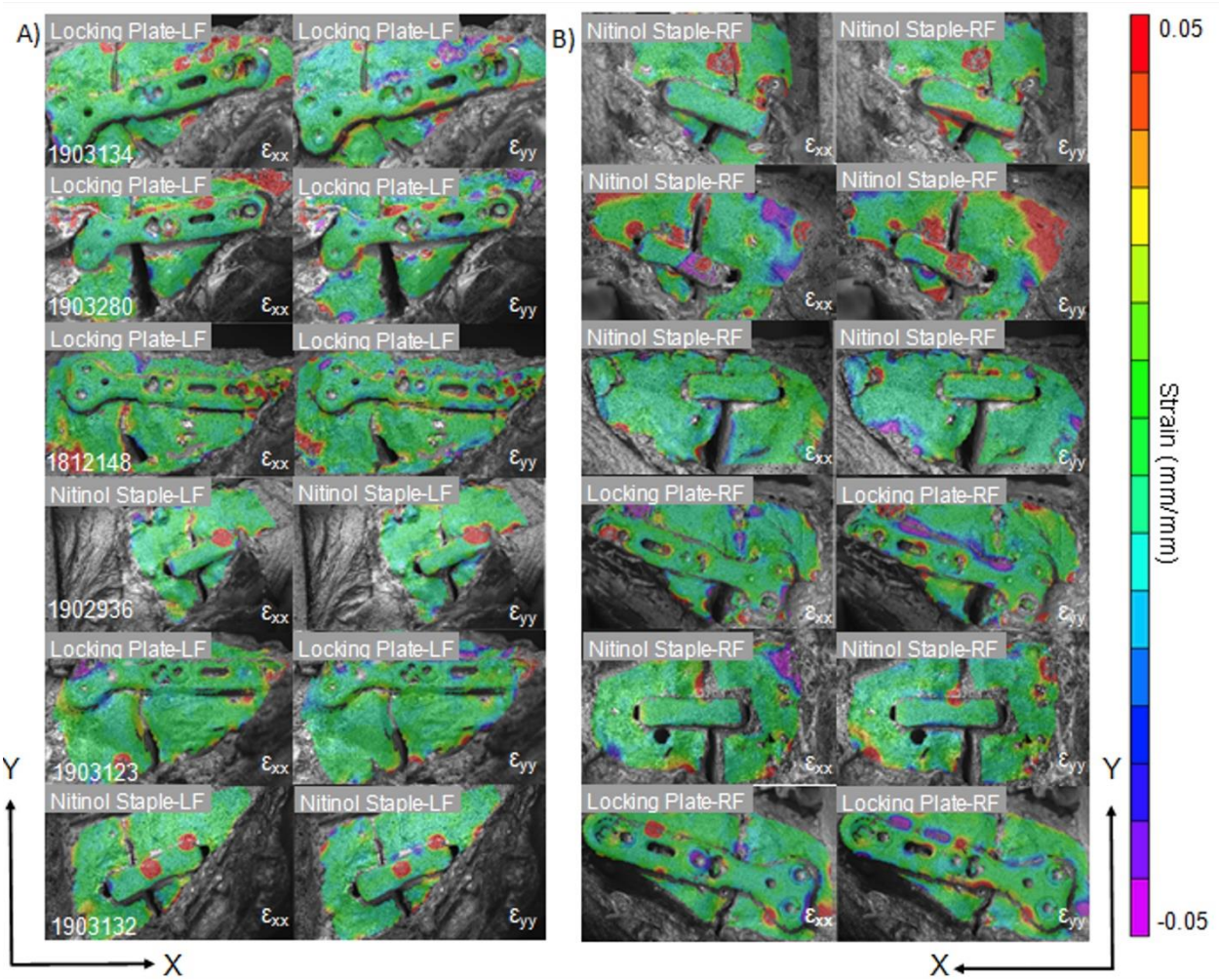

Figure 13. 3D-DIC strain map of cadaveric samples after anthropomorphic loading [41]

5.2 **Measured Gapping at the 1st TMT**

Figure 14b presents the gap displacement over time, showing the gradual opening for each implant and individual test. Gap displacement was measured by DIC by tracking separation between two points of the bone on either side of the joint. A maximum gap opening of ~4mm was observed between the locking plate and nitinol staple constructs during testing. By the 100th cycle, the locking plate samples gapped an average of ~2.2mm while the nitinol staples gapped an averaged ~3.2mm under maximum load of 50 N. After loading was removed, marked by the 120th cycle, the locking plate samples averaged ~0.8mm of residual gapping and the nitinol staple samples averaged ~0.3mm of residual gapping. This indicates that, while there is variability with initial gap displacement during loading, final plantar gapping is more reproducible. Another takeaway from this work was that there is a relationship between the implant location, the amount of gapping and strain measured at the 1st TMT joint. The proximity of the locking plate to the dorsal side of the toe allowed larger displacements and a smaller variation in bone strain was measured (Figure 14). On the contrary, more plantar insertion resulted in smaller gap distance with a larger variation in bone strain. A plantar fixation location has also been shown to decrease the presence of metalware. The reduction in metalware prominence inherently lowers the risk of related bursitis forming at the TMT joint [38]. Locking Plate 2 (P2) is inserted more plantarly across the first TMT joint and exhibited the smallest gap displacement following testing while Locking Plate 1 (P1) and Locking Plate 3 (P3) were more dorsal relative to the cross screw and resulted in larger gap displacements. For the nitinol staples, more plantar placement of the EL-1818S2 across the TMT joint, seen in Nitinol Staple 1 (NS1), resulted in smaller gap displacement. EL-1818S2 was placed more dorsally, as for Nitinol Staple 2 (NS2) and Nitinol Staple 3 (NS3) and experienced similar larger gap profiles. One difference is that the nitinol staple strain profiles in Figure 14 remained linear regardless of implant location.

Another note is that a linear negative strain measured in the x-direction of the nitinol staples indicates that the staple was able to apply and maintain constant compression of the joint across all cycles of testing [34].

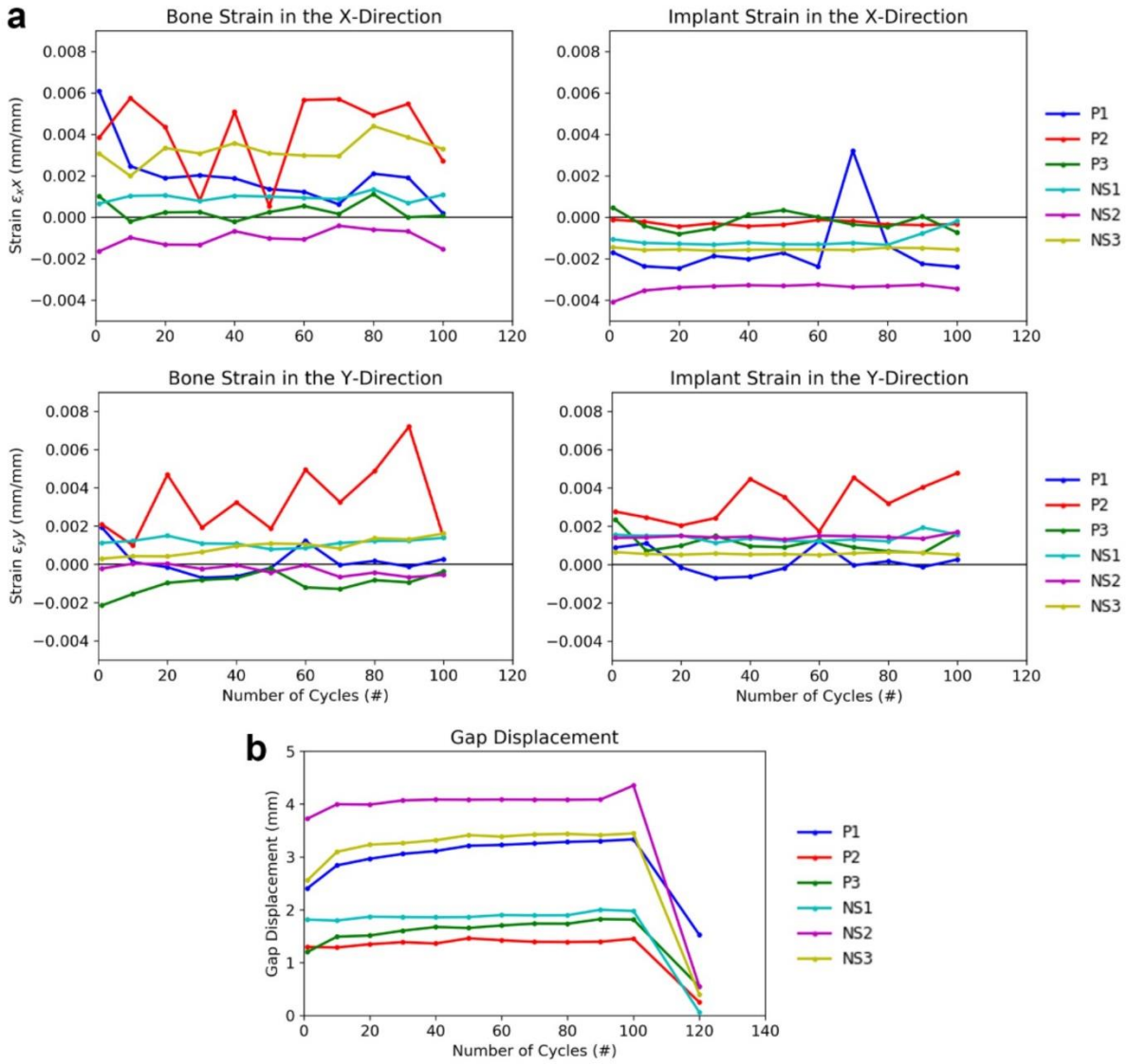

Figure 14. Quantification of a) strain and b) TMT gap displacement measured during maximum load (50N) and residual gapping [34]

Six matched-pair cadavers were tested for a total of 12 samples. The specific bone densities and implant assignments are given in Table I. Only one matched pair, Donor 1903280,

did not sustain the full 100 iterations of cyclic loading to 50N due to the poor bone quality. The displacement was measured via DIC by tracking separation between two points of the bone on either side of the TMT joint [41].

Table I. Donor information for each cadaver purchased from MedCure [41]

Donor #	Age	Sex	BMD (LF/RF) g/cm^2	Max Gap (LF/RF) mm	Max E_{xx} strain (LF/RF) mm/mm	Max E_{yy} strain (LF/RF) mm/mm	Max E_{xy} (LF/RF) mm/mm	Implant (LF/RF)
1902936	76	M	0.82/0.82	2.07/1.74	0.51/0.23	0.36/0.013	0.25/0.11	Staple/Plate
1903123	72	M	1.07/1.04	1.78/0.77	0.02/0.02	0.01/0.04	0.006/0.002	Plate/Staple
1903132	69	F	0.87/0.87	1.59/1.06	0.24/0.08	0.11/0.022	0.046/0.021	Staple/Plate
1903134	47	M	1.0/0.89	1.03/0.32	0.09/0.24	0.018/0.22	0.015/0.008	Plate/Staple
1903280	91	F	0.45/0.42	2.31/1.12	0.08/0.42	0.07/0.34	0.004/0.011	Plate/Staple
1812148	67	M	0.91/0.92	3.90/3.18	0.04/0.03	0.03/0.015	0.028/0.004	Plate/Staple

Maximum gap openings of 3.1 mm and 3.9 mm was observed for the locking plate and nitinol staple constructs, respectively, during testing. Traditionally, 3 mm has been used as the threshold displacement indicative of surgical construct failure. We quantified the differential recovery of both constructs in this work, using the dynamic capabilities of DIC technology, and found that the nitinol staple construct averaged 2.116 ± 0.893 mm of gapping under maximum load, while the locking plate construct averaged 1.367 ± 0.917 mm under maximum load. When comparing all nitinol staple constructs against the locking plate constructs, we did see a significant difference in gapping ($P = 0.001$). Further group comparisons between the left and right feet of male and female did not yield any significance differences ($P = 0.077$ and $P = 0.45$, respectively). By comparing the gender of the cadaveric samples, we did see a significant

difference during maximum load (P = 0.048). Figure 15 demonstrates the locking plate samples recovered to an average of 0.3898 ± 0.378 mm of residual gapping at the 1st TMT, while nitinol staple samples averaged 0.673 ± 0.546 mm. Once again, there was a significant difference in residual gapping between nitinol staple constructs against the locking plate constructs (P = 0.044) [41].

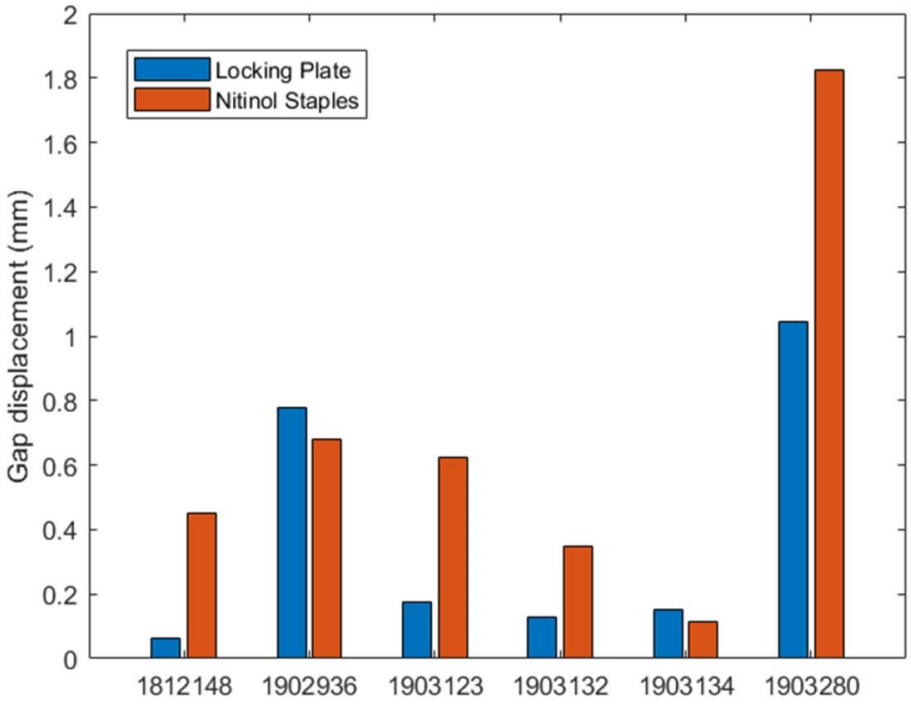

Figure 15. TMT gap displacement measured at final residual gapping

Comparisons between left and right feet of male and females did not yield any significance difference in residual strain (P = 0.073 and P = 0.34, respectively). There also was a lack of a significant difference in performance during maximum load (P = 0.077) when strictly comparing gender. The results demonstrated that the locking plates provided better gap resistance under load across a range of bone densities. Figure 16 shows the correlation between bone density of the cadaveric samples and the measured gapping during loading. Repeated loading cycles strained the bone and TMT joint, weakened the interface between the bone and implant, and allowed the joint gap to enlarge, as shown in Figure 15. However, there were higher

regions of strain localized at the bridge and legs of the staple seen in Figures 17 and 20. In order to better understand the strain contours, Figure 18 included displacement in the X, Y, and Z directions. Figure 19 served as a representative plot of the distinct difference in the strain experienced between the nitinol staple and locking plate in Donor 1903132. Figures 20 and 21 show a strain range of -0.05 to 0.05 mm/mm and reveal low-magnitude strain locations in the test samples [41].

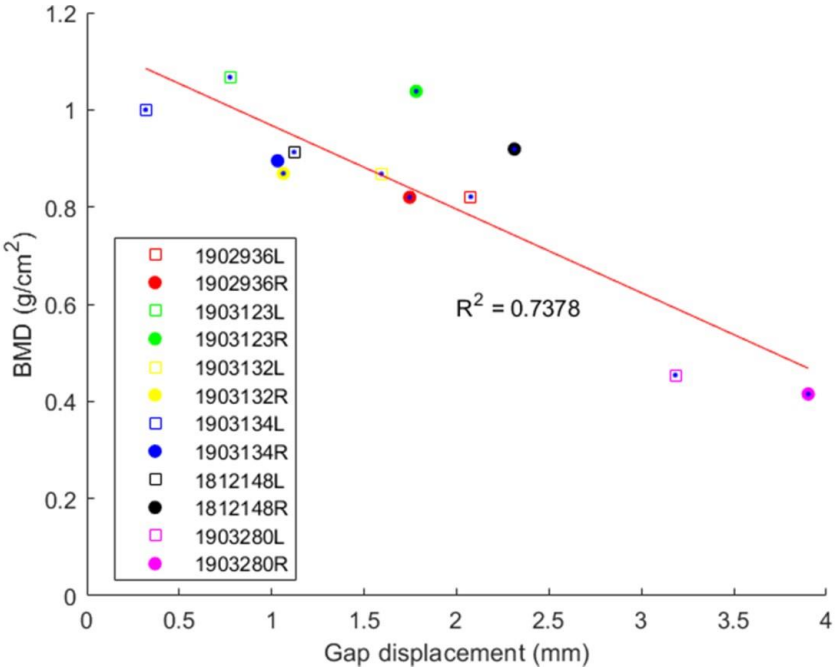

Figure 16. Correlation (R^2 = 0.7378) between bone density and measured gap. [41]

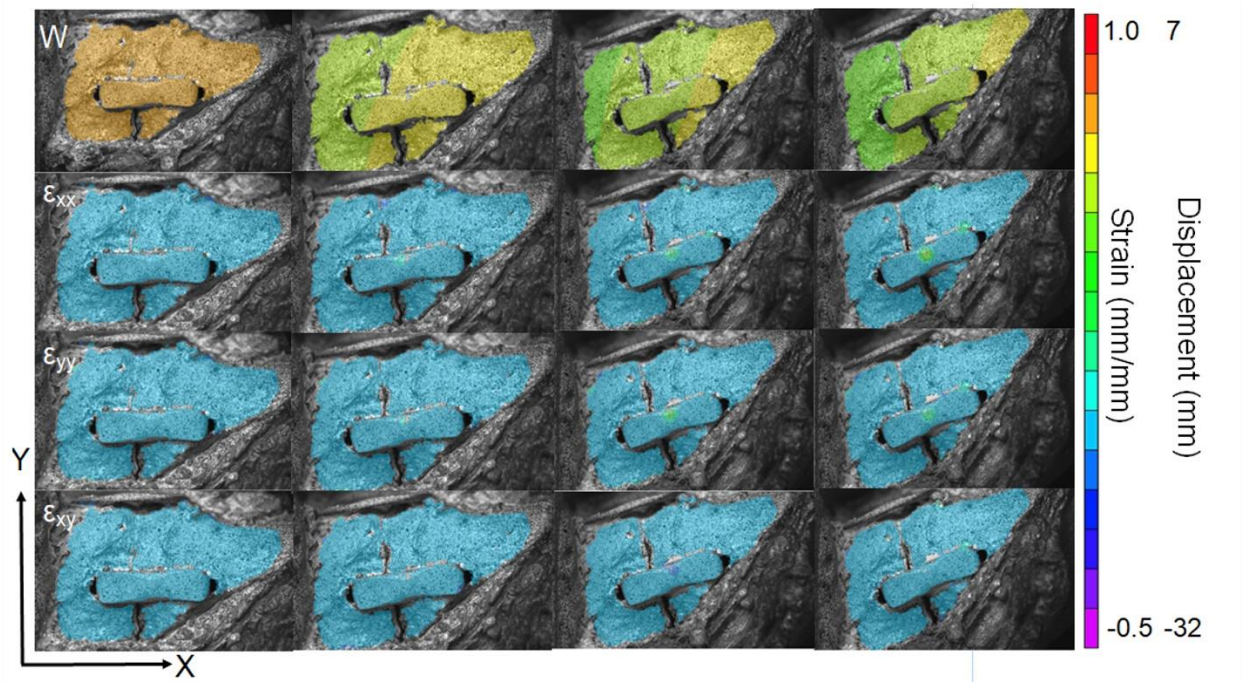

Figure 17. Representative strain map (e_{xx}, e_{yy}, e_{xy}) of Donor 1903132 against displacement in the Z plane at various time points ending in 50-N load of the 100th cycle (from left to right). The subimage dimensions are 50mm x 32mm. [41]

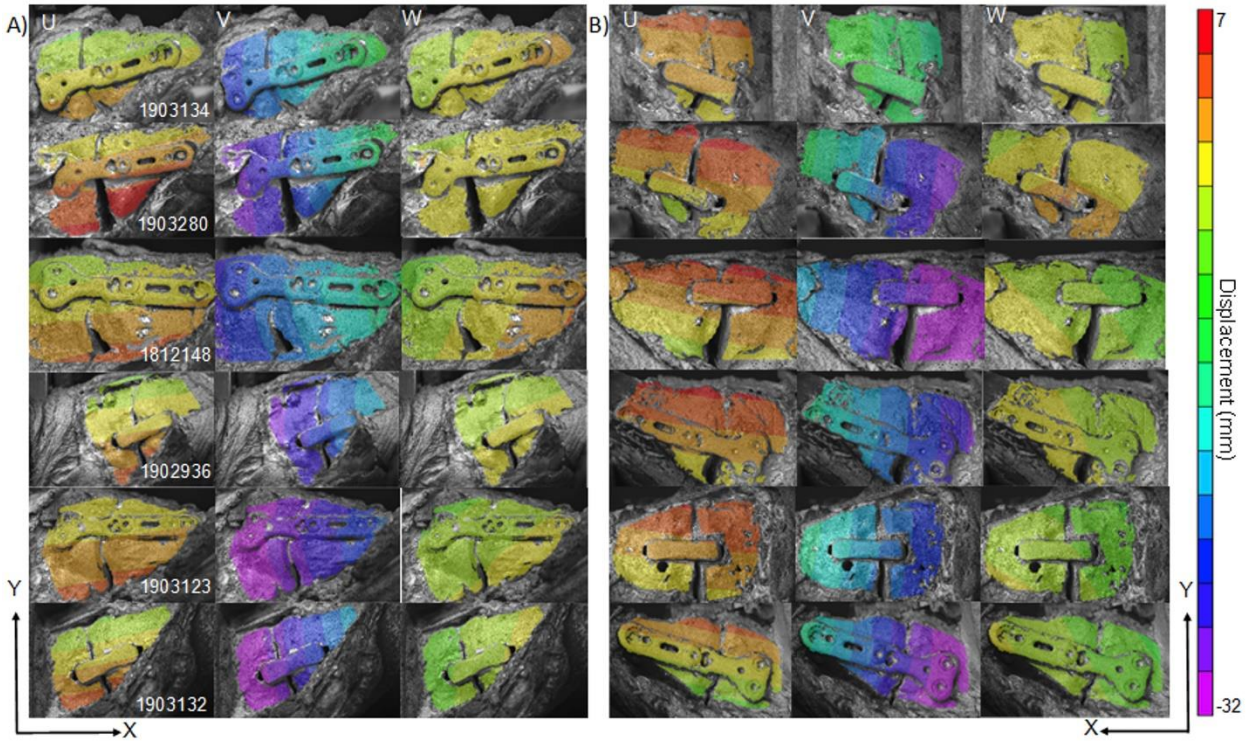

Figure 18. Displacement maps of (a) left foot and (b) right foot of six matched-pair donors, with randomized implant selection per foot. Each sample is shown at 50N of their last cycle. The subimage dimensions are 48mm x 30mm. [41]

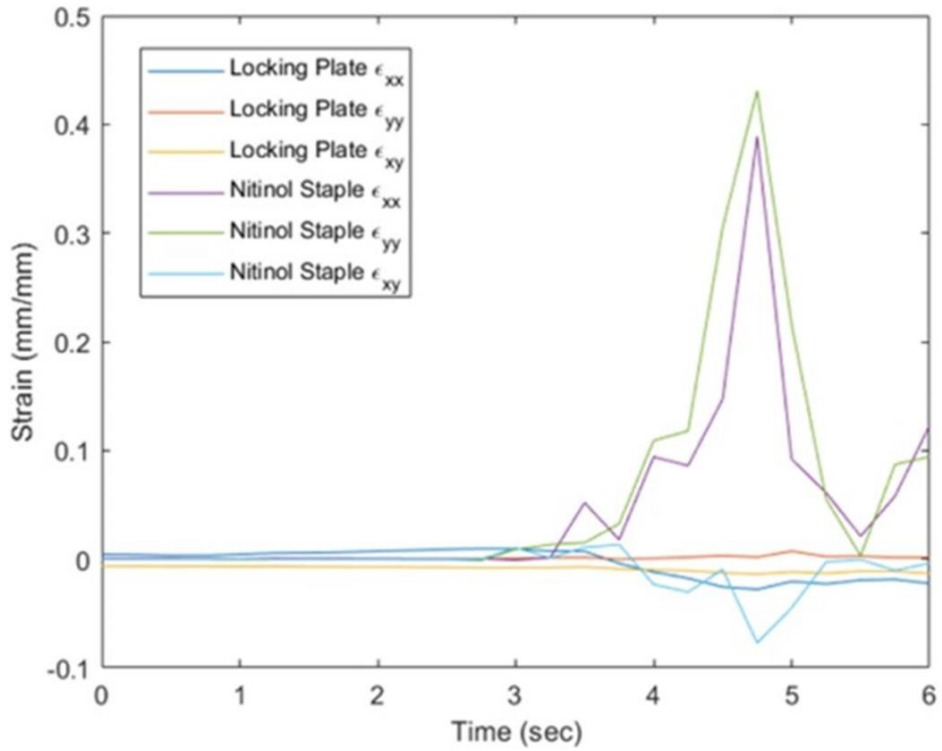

Figure 19. Strain measured at various time points in Donor 1903132 during a single loading cycle with nitinol staples and locking plate implant systems. [41]

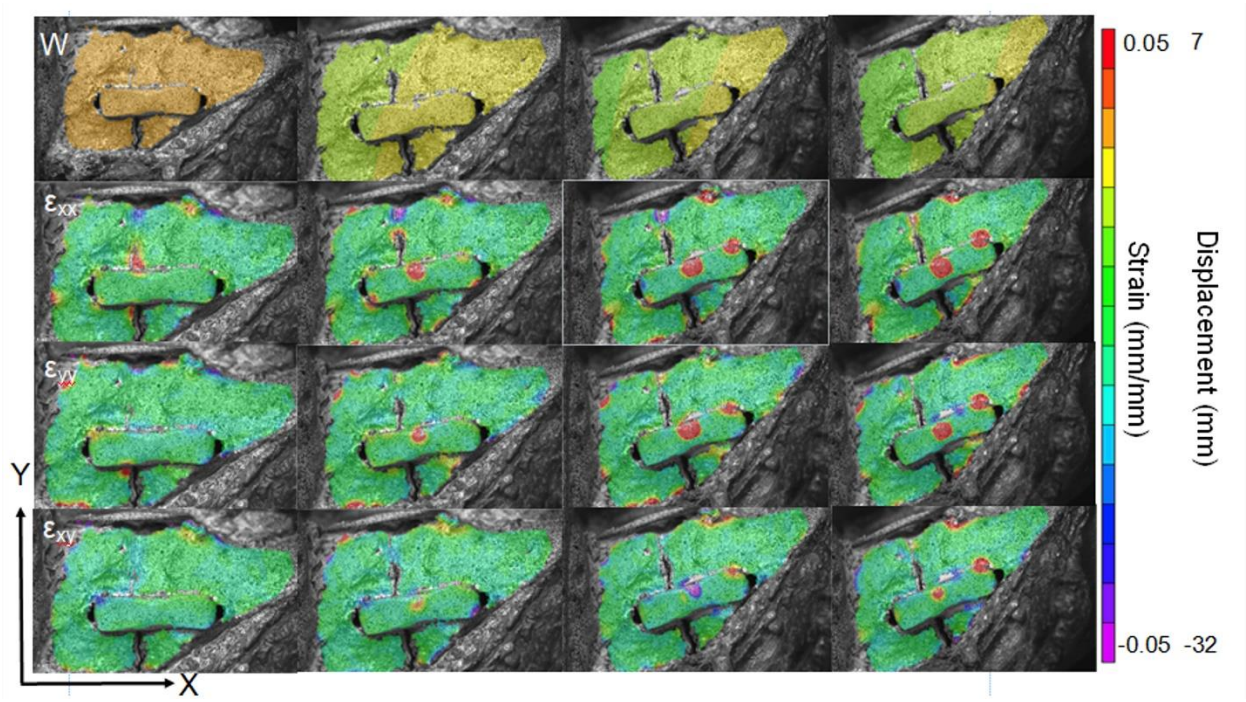

Figure 10. Representative strain map (e_{xx}, e_{yy}, e_{xy}) of Donor 1903132 against displacement in the Z plane in various time points at a smaller strain range to reveal small-magnitude strains. The subimage dimensions are 50mm x 32mm. [41]

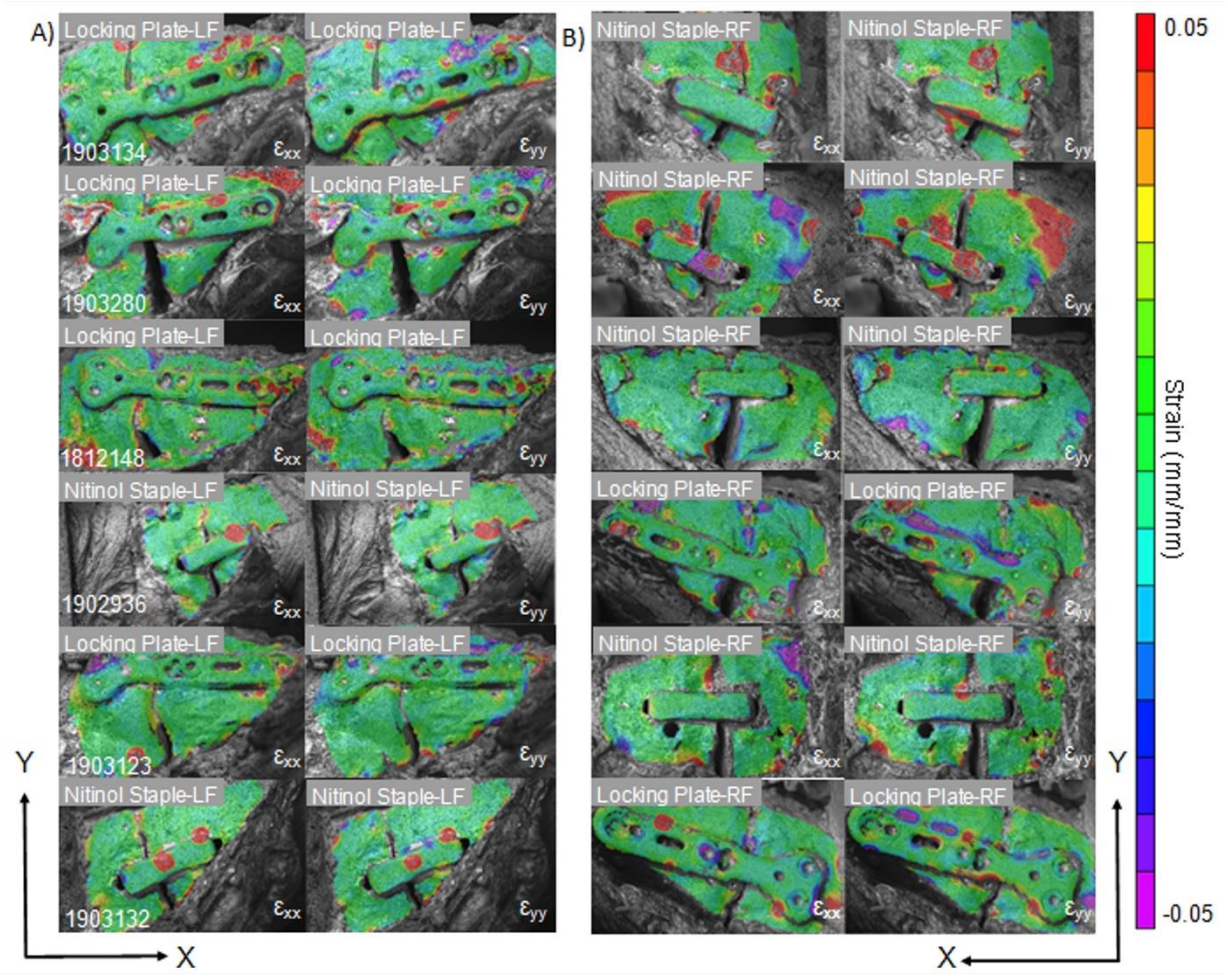

Figure 11. DIC strain maps of (a) left foot and (b) right foot of six matched pairs of donors at a smaller strain range to reveal small-magnitude strains. [41]

Chapter 6: Conclusions

In this work, the sawbone phase was the first to demonstrate the use of in-situ 3D-DIC to evaluate the performance of implant and bone substitutes during cyclical loading. Mechanical testing via the aluminum rod validation study yielded results analogous to traditional symmetric bend tests and can serve as a baseline for future studies that implement asymmetric bend. The use of an asymmetric bend test introduced a load profile that was more anthropomorphic. Cyclical load tests were completed with polyurethane foot models following a simulated arthrodesis using either a locking plate and lag screw system or dual nitinol staples. 3D-DIC

profiles revealed that nitinol staple implants had better strain distribution with minimal strain concentrations along the implant-bone interface, which was readily observed for locking plates. Nitinol staples also exhibited superior compressive ability even after all load was removed and had an average residual TMT joint gap displacement of 0.3mm compared to 0.8mm for the locking plate system. Plantar positioning of the implants showed marked improvement in reduction of gapping for both implant types when compared to a more medial or dorsal implant position. Tests showed that the locking plate's proximity towards the dorsal side of the toe allowed for larger displacements and a smaller variation in bone strain. In contrast, a more plantar insertion of the implant resulted in a smaller gap distance with a larger variation in bone strain [34].

The cadaver phase further pushed the limits of 3D-DIC application in evaluating implant performance while operating within a new sample preparation methodology designed for the presence of biological tissue. Contrary to the sawbone phase, the locking plate constructs provided statistically superior performance during loading compared to the nitinol staple constructs. The resulting DIC profiles revealed that the locking plate distributed strain more effectively, reducing the magnitude of strain concentrations and gapping along the implant–bone interface compared to the nitinol staples [41]. The difference in strain profiles suggest bone density plays a larger role in the implant's performance than what was previously understood.

With the innovative test setups detailed in this work, additional research is warranted to study the relationship between the implant location, bone density, and the amount of gapping and strain measured at the first TMT joint until hardware fracture. In order to reduce the financial burden from hallux valgus procedures, implants must have well established patient parameters (bone density, gender, weight) to allow for the highest chance of union at the 1st TMT joint.

While this work indicated that the locking plate represented a more appropriate implant for joint arthrodesis across a range of bone densities, the nitinol staples have patented delivery devices which allow for rapid insertion once the joint is provisionally reduced [39,40,41]. Locking plate systems require a more complex installation and take several minutes following joint alignment. The author hopes that this work will help spur the next push in development of improved implant technology as well as improve surgical understanding on how to best match each type of hallux valgus implant to patient specific criteria.

References

1. Nix S, Smith M, Vicenzino B. "Prevalence of hallux valgus in the general population: a systematic review and meta-analysis." Journal of Foot and Ankle Research 3(21), 1–9. 2010.

2. Hurn SE, Vicenzino B, Smith MD. "Functional Impairment Characterizing Mild, Moderate and Severe Hallux Valgus." Arthritis Care & Research 67(1), 80-88. 2015.

3. Willey JC, Reuter LS, Belatti DA, Phisitkul P, Amendola N. "Availability of consumer prices for bunion surgery." Foot & Ankle International 35(12), 1309-1315. 2014.

4. Scranton PE, Coetzee JC, Carreira D. "Athrodesis of the first metatarsocuneiform joint: a comparative study of fixation methods." Foot & Ankle International 30(4), 341–345. 2009.

5. Wülker N, Mittag F. "The Treatment of Hallux Valgus." Dtsch Arztebl Int 109(49), 857-868. 2012.

6. Bredbenner TI, Haug RH. "Substitutes for human cadaveric bone in maxillofacial rigid fixation research." Oral Surgery, Oral Medicine, Oral Pathology, Oral Radiology, and Endodontology 90(5), 574-580. 2000.

7. Galois L. “History of surgical treatments for hallux valgus.” European journal of orthopaedic surgery & traumatology : orthopedie traumatologie 28(8) 1633-1639. 2018.

8. Lee KM, Ahn S, Chung CY, Sung KH, Park MS. “Reliability and Relationship of Radiographic Measurements in Hallux Valgus.” Clinical Orthopaedics and Related Research 470(9), 2613-2621. 2012.

9. Chi TD, Davitt J, Younger A, Holt S, Sangeorzan BJ. “Intra- and inter-observer reliability of the distal metatarsal articular angle in adult hallux valgus.” Foot & Ankle International 23(8), 722-726. 2002.

10. Symeonidis PD, Anderson JG. “Original and Modified Lapidus Procedures: Proposals for a New Terminology.” Journal of Bone and Joint Surgery 103(4), 1-7. 2021.

11. Coughlin MJ, Jones CP, Viladot R, Glano P, Grebing BR, Kennedy MJ, Shurnas PS, Alvarez F. “Hallux Valgus and First Ray Mobility: A Cadaveric Study.” Foot & Ankle International 25(8), 537-544. 2004.

12. Ellington JK, Myerson MS, Coetzee JC, Stone RM. “The use of the Lapidus procedure for recurrent hallux valgus.” Foot & Ankle International 32(7), 674-680. 2011.

13. So E, Van Dyke B, McGann MR, Brandao R, Larson D, Hyer CF. “Structures at Risk from an Intermetatarsal Screw for Lapidus Bunionectomy: A Cadaveric Study.” Journal

of Foot & Ankle Surgery 58(1), 62-65. 2018.

14. Sutton MA, Orteu JJ, Schreier HW. *Image Correlation for Shape Motion and Deformation Measurements*. Springer Science, New York. 2009.

15. Rossol MN, Shaw JH, Bale H, Ritchie RO, Marshall DB, Zok FW. "Characterizing weave geometry in textile ceramic composites using digital image correlation." Journal of the American Ceramics Society 96(8), 2362–2365. 2013.

16. Ghorbani R, Matta F, Sutton MA. "Full-field deformation measurement and crack mapping on confined masonry walls using digital image correlation." Experimental Mechanics 55(1), 227-243. 2014.

17. Helm JD, McNeil SR, Sutton MA. "Improved three-dimensional image correlation for surface displacement measurement." Optical Engineering 35(7), 1911-1920. 1996.

18. Sutton MA, Yan J, Deng X, Cheng CS, Zavattieri PD. "Three-dimensional digital image correlation to quantify deformation and crack-opening displacement in ductile aluminum under mixed mode I/III loading." Optical Engineering 46(5), 1-17. 2007.

19. Sztefek P, Vanleene M, Olsson R, Collinson R, Pitsillides AA, Shefelbine S. "Using digital image correlation to determine bone surface strains during loading and after

adaptation of the mouse tibia." Journal of Biomechanics, 43(4), 599-605. 2010.

20. Steiner M, Volkheimer D, Meyers N, Wehner T, Wilke HJ, Claes L, Ignatius A. "Comparison between different methods for biomechanical assessment of ex vivo fracture callus stiffness in small animal bone healing studies." PLoS One 10(3), 1-16, 2015.

21. Kubiak EN, Fulkerson E, Strauss E, Egol KE. "The Evolution of Locked Plates." Journal of Bone and Joint Surgery 88, 189-200. 2006.

22. Klos K, Gueorguiev B, Mückley T, Fröber R, Hofmann GO, Schwieger K, Windolf M. "Stability of medial locking plate and compression screw versus two crossed screws for lapidus arthrodesis." Foot & Ankle International 31(2), 158-163. 2010.

23. Aiyer A, Russell NA, Pelletier MH, Myerson M, Walsh WR. "The Impact of Nitinol Staples on the Compressive Forces, Contact Area, and Mechanical Properties in Comparison to a Claw Plate and Crossed Screws for the First Tarsometatarsal Arthrodesis." Foot & Ankle Specialist 9(3), 232-240. 2016.

24. Hoon QJ, Pelletier MH, Christou C, Johnson KA, Walsh WR. "Biomechanical evaluation of shape-memory alloy staples for internal fixation-an in vitro study." Journal of Experimental Orthopaedics 3(1), 19-29. 2016.

25. Nagaraja S, Palepu V. "Comparisons of anterior plate screw pullout strength between polyurethane foams and thoracolumbar cadaveric vertebrae." Journal of Biomechanical Engineering 138(10), 1-6. 2016.

26. O'Neill F, Condon F, McGloughlin T, Lenehan B, Coffey C, Walsh M. "Validity of synthetic bone as a substitute for osteoporotic cadaveric femoral heads in mechanical testing: a biomechanical study." Bone & Joint Research 1(4), 50-55. 2012.

27. Patel PSD, Shepherd DET, Hukins DWL. "Compressive properties of commercially available polyurethane foams as mechanical models for osteoporotic human cancellous bone." BMC Musculoskeletal Disorders 9(137), 5-11. 2008.

28. Scott AT, DeOrio JK, Montijo HE, Glisson RR. "Biomechanical comparison of hallux valgus correction using the proximal chevron osteotomy fixed with a medial locking plate and the Ludloff osteotomy fixed with two screws." Clinical Biomechanics 25(3), 271-276. 2010.

29. Shim V, Boheme J, Josten C, Anderson, I. *Polyurethane*. InTech, Croatia. 2012.

30. Apostol DA, Constantinescu DM, Marsavina L, Linul E. "Mixed-Mode Testing for an Asymmetric Four-Point Bending Configuration of Polyurethane Foams." Applied

Mechanics and Materials 760, 239-244. 2015.

31. Whaley RE. "Fatigue and static strength of notched and unnotched aluminum-alloy and steel specimens." Experimental Mechanics 2(11), 329-334. 1962.

32. Bauchau OA, Craig JI. *Structural Analysis*. Springer, Netherlands. 2009.

33. Aerospace Specification Metals Inc. (n.d.). ASM material data sheet aluminum 6061-T6. [online] Available at: https://asm.matweb.com/search/SpecificMaterial.asp?bassnum=ma6061t6

34. Shen VC, Bumgardner CH, Actis L, Ritz J, Park J, Li X. "3D Digital Image Correlation Evaluation of Arthrodesis Implants." Clinical Biomechanics 71(1), 29-36. 2020.

35. Luger EJ, Nissan M, Karpf A, Steinberg EL, Dekel S. "Patterns of weight distribution under the metatarsal heads." Journal of Bone & Joint Surgery 81(2), 199-202. 1999.

36. Cottom JM, Baker JS. "Comparison of Locking Plate with Interfragmentary Screw Versus Plantarly Applied Anatomic Locking Plate for Lapidus Arthrodesis: A Biomechanical Cadaveric Study." Foot & Ankle Specialist 10(3), 227-231. 2017.

37. Blitz NM. “Addressing Common Complications of the Lapidus Bunionectomy.” Podiatry Today 29(2), 50-55. 2016.

38. Goldbloom D, Makwana N, Laing P, Toullec E, Graff W, Charbel A. “A new ‘tension side’ locking plate for Hallux Valgus: A prospective multicentre case series.” Foot & Ankle Surgery 22(2), 103-108. 2016.

39. Schipper ON, Ford SE, Moody PW, Van Doren B, Ellington JK. “Radiographic Results of Nitinol Compression Staples for Hindfoot and Midfoot Arthrodeses.” Foot & Ankle International 39(2), 172-179. 2018.

40. Dock CC, Freeman KL, Coetzee JC, McGaver RS, Giveans MR. “Outcomes of Nitinol Compression Staples in Tarsometatarsal Fusion.” Foot & Ankle Orthopaedics 5(3), 1-6. 2020.

41. Shen VC, Bumgardner CH, Actis L, Park J, Moyer D, May-Nikstaitis K, Li X. “In Situ Deformation of First Tarsometatarsal Arthrodesis Implants with Digital Image Correlation: A Cadaveric Study.” The Minerals, Metals & Materials Society 74(9), 3357-3366. 2022.